Design of a 3D Printed Force Sensor in the Field of Robotics Utilizing an Embedded Constantan Wire as Sensing Element

Nikolai Hangst, Jan Müllerleile, Thomas M. Wendt, Lukas Stiglmeier, Philipp Gawron, Urban B. Himmelsbach, and Anke Fischer, Offenburg University of Applied Sciences, Work-Life Robotics Institute, 77652 Offenburg, Germany

Abstract

The development of a 3D printed force sensor for a gripper was studied applying an embedded constantan wire as sensing element. In the first section, the state of the art is explained. In the main section of the paper the modeling, simulation and verification of a sensor element are described for a three-point bending test made in accordance with the DIN EN ISO 178. The 3D printing process of the Fused Filament Fabrication (FFF) utilized for manufacturing the sensor samples in combination with an industrial robot are shown. A comparison between theory and practice are considered in detail. Finally, an outlook is given regarding the integration of the sensor element in gripper jaws.

1 Introduction

3D printing has been continuously developed in research institutions and technology companies in the recent years. In particular, the trend towards complex and functional components, or even the printing of complete mechatronic systems provides a major technological advance [1-5].
3D printing of functional components is also important in the field of robotics, especially in the domain of gripping systems for industrial and collaborative robotics [6]. In classical robotics, it is desired to avoid damage to sensitive and fragile components by utilizing embedded sensors [7-9]. In collaborative robotics, an additional differentiation between humans and the component to be gripped is required [7-8, 10-11]. Another reason for using 3D printing is the freedom that it provides in the design of products [8, 10, 12-13]. By using 3D printing it is possible to fabricate individual gripper jaws, including sensors and adapted gripping surfaces in a single process. This process is called multi-material printing [14-15].
3D printed force sensors have been investigated in this research area [4]. These includes sensors in the area of gripping jaws [6, 14-15]. The most commonly utilized force sensors are based on strain gauge technologies. This works on the principle of resistance change as a result of stretching or compression [4]. The sensors consist of a non-conductive and a conductive material [4, 14]. The non-conductive material are typically plastics such as acrylonitrile butadiene styrene (ABS) for rigid grippers or thermoplastic polyurethane (TPU) for flexible grippers [4, 14-15]. Conductive plastics or silver inks are often utilized as the conductive material [4, 14]. To obtain a printable conductive plastic, conductive particles like carbon or graphene are added to it [4, 14-15].
The efficiency of force sensors is directly related to its material properties, as well as its structural design [4]. Plastic substrate has the disadvantage of a decrease mechanical load capacity [16]. In addition, plastics have viscoelastic properties. This may lead to creep of the material under a mechanical load. A residual strain is also possible when the material is relieved again after a load has been applied. Consequently, the measured value of the sensor will be permanently distorted [4]. Furthermore, plastics show a high thermal expansion, which is about 10 times higher compared to metals [17]. All these disadvantages show that the 3D Printing of a force sensor has been so far unsuitable for the industrial market.
As demonstrated by Rashid and Koç, continuous fiber reinforcement can be applied to increase the mechanical load capacity and at the same time reduce the viscoelastic behavior [18]. According to Dickson et al., even higher tensile strengths can be achieved compared to aluminum [16]. The reduced viscoelastic behavior is related to a reduced strain of the polymer chains. This lowers the stress in the plastic and the sliding of the polymer molecules. Continuous fibers also increase the Young's modulus of the base material. This allows it to return to its initial position more easily [18]. Considering to thermal expansion, correct arrangement of the fibers can reduce the expansion in certain directions. Deformations already occur during 3D printing as a consequence of cooling material. This results in residual stresses in the base material. By using the continuous fibers, this can be counteracted [19].
In this paper a first 3D printed force sensor utilizing a constantan wire as the sensing element is presented. The work was to demonstrate an alternative to a force sensor made of pure plastic. A sensor was created that served as a force sensor as well as continuous fiber reinforcement. Another advantage of this sensor construction are the known parameters of constantan. To the best of the authors knowledge, a sensor of this type doesn´t exist so far. It represents a new approach in the field of 3D printed sensor technology.

2 Materials and Methods

2.1 Materials and Machines

As non-conductive material polyethylene terephthalate glycol (Prusament PETG Signal White [20], Prusa Research) was utilized. The conductive material was a constantan wire (CuNi44, DM 0.2 mm, VDM-Metals). The non-conductive geometry was 3D printed

ISBN 978-3-8007-5835-7

(Prusa MINI, ND 0.4 mm) while the constantan wire was embedded with a robot (Hiwin RA-605, Hiwin). The robot utilized a special tool.

2.2 Developed Tool

At the beginning, it was necessary to develop a tool to embed a constantan wire into a 3D printed part. This tool uses a stepper motor to feed the wire through a E3D Lite 6 Hotend Bowden from E3D. During this process, the material is pressed against the drive gear of the stepper motor by a preloaded ball bearing. The installed nozzle is made of messing and has a diameter of 0.3 mm. A servo DS3012 MG with an adaptive cutting blade was installed for cutting the wire after it is embedded. The coiled material can be fixed on a holder. The tool is shown in **Fig. 1**.

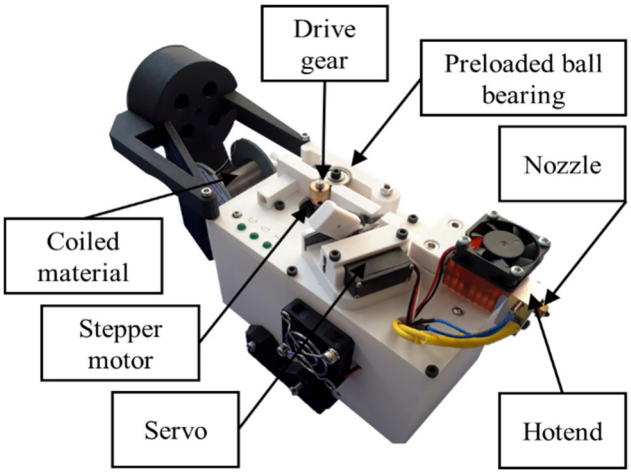

Figure 1 Assembled tool utilized for embedding the constantan wire

2.3 Sensor Design

The sensor was made of PETG. The part dimensions from DIN EN ISO 178 were taken for a three-point bending test. For a high sensitivity, the wire must be embedded close to the surface and was placed at a height of 2.5 mm. The component was inverted for the bending test to apply a tensile force to the sensing element.

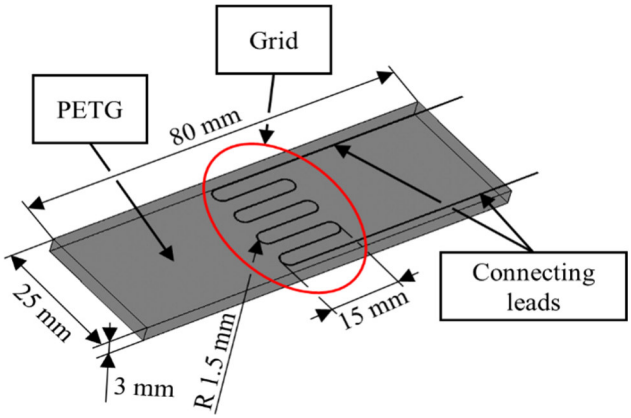

Figure 2 Sensor Design

The force sensor consists of a meander-shaped grid with six embedded resistance paths, excluding the connecting leads. The wire is mainly kept in position by the reverse loops. Therefore, the two connecting leads up to the first reversing loop are not included in the calculations of the resistance change. The Design of the sensor is shown in **Fig. 2**.

2.4 Sensor Modeling

Fig. 3 shows the load case of the sensor. In the mid-section of the beam between x_2 and x_5, it is a composite material consisting of PETG and constantan. The calculation of the sensor´s behavior was separated into a mechanical and an electrical part. Firstly, the required force for the deflection of the beam and the resulting change in strain of the sensor grid were calculated. Subsequently, the strain of the sensor wire and the associated resistance change could be determined. Due to symmetry reasons, it is sufficient to utilize the left part of the beam from x_1 to x_F.

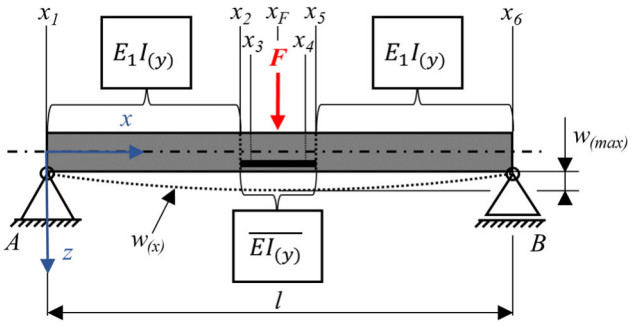

Figure 3 Modeling Sketch of the sensor

The beam theory according to Euler-Bernoulli and Timoshenko was first applied to the mechanical part. The general equation for the bending beam is expressed as (1):

$$w_{(x)} = w_{b(x)} + w_{S(x)} \tag{1}$$

$w_{(x)}$ represents the entire bending line of the beam, $w_{b(x)}$ is the bending line of the shear rigid part according to Euler-Bernoulli and $w_{S(x)}$ is the consideration of shear stresses based on Timoshenko. For the calculation of the Euler-Bernoulli contribution the following basic equation is valid for the part between x_1 and x_2 as well as x_5 and x_6 (2):

$$E_1 I_{(y)} \ddot{w}_{b(x)} = -M_{(x)} \tag{2}$$

E_1 is the Young's modulus of the single material, $I_{(y)}$ is the second moment of area, $\ddot{w}_{b(x)}$ is the second-order derivation of the bending line and $M_{(x)}$ is the resultant bending moment. According to Euler-Bernoulli, the following basic equation applies to the composite material between x_2 and x_5 (3):

$$\overline{EI_{(y)}} \ddot{w}_{b(x)} = -M_{(x)} \tag{3}$$

Equation 3, with the exception of the different Young's modulus and second moment of area, is similar to

Equation 2. However, the expression can be expressed in terms of the Young's modulus of material 1 (4):

$$E_1\overline{I_{(y)}} = \overline{EI_{(y)}} \tag{4}$$

$\overline{I_{(y)}}$ represents the second moment of area of the composite material, which is formed by an equivalent area. The new cross section is assumed to be made completely of material 1. The area of material 2 is scaled. For the part of the beam between x_2 and x_F, Euler-Bernoulli gives the final following formula (5):

$$w_{b(x)} = -\frac{Fx^3}{12E_1\overline{I_{(y)}}} + \frac{Fl^2x}{16E_1\overline{I_{(y)}}} + \frac{1331Fl^3}{196608E_1}\left(\frac{1}{I_{(y)}} - \frac{1}{\overline{I_{(y)}}}\right) \tag{5}$$

The values of the integration constants of the differential equations can be calculated utilizing suitable boundary conditions. For the calculation of the Timoshenko part the following basic equation is valid for the part between x_1 and x_2, as well as between x_5 and x_6 (6):

$$KG_{(1)}A\dot{w}_{S(x)} = Q_{(x)} \tag{6}$$

K is the shear correction factor, $G_{(1)}$ is the shear modulus of the single material, A is the cross section area, $\dot{w}_{S(x)}$ is the first-order derivation of the bending line and $Q_{(x)}$ is the resulting shear force. According to Timoshenko, the following basic equation can be applied for the composite material between x_2 and x_5 (7):

$$KGA\dot{w}_{S(x)} = Q_{(x)} \tag{7}$$

Equation 7 with the exception of the shear modulus is similar to equation 6. The new shear modulus is generated from the composite material. For the beam part between x_2 and x_F Timoshenko's approach gives the following formula (8):

$$w_{S(x)} = \frac{Fx}{2KGA} + \frac{Fx}{2KA}\left(\frac{1}{G_1} - \frac{1}{G}\right) \tag{8}$$

The values of the integration constants of the differential equations can also be calculated utilizing suitable boundary conditions. Equation 5 and 8 can be introduced into equation 1. For the calculation of the force F in dependence of the maximum deflection $w_{(max)}$, the equation 1 must be rearranged according to this force. Afterwards, the strain changes of the middle part from x_2 to x_5 can be calculated by utilizing the following formula (9):

$$\varepsilon_i = \frac{\frac{1}{x_{i2} - x_{i1}}\int_{x_{i1}}^{x_{i2}} M_{(x)}dx}{\overline{W}E_w} n_w l_{xi1,2} \tag{9}$$

ε_i is the length change in mm, x_{i1} and x_{i2} are the integration limits, $M_{(x)}$ is the resulting bending moment, $\overline{W}$ is the section modulus from the composite material, E_w is the tensile modulus from the wire, n_w is the scale factor based on the ratio of the individual tensile moduli and $l_{xi1,2}$ is the length between the integration limits. For the sensor grid there are three areas to be considered. The wire in the area from x_3 to x_4 is linearly aligned. In this case, no further action is required. The reverse loops are located between x_2 and x_3 as well as between x_4 and x_5. Consequently, this length change must be converted to an elliptical shape. The approximation equation according to Rumanujan is suitable for this. After the mechanics were considered, the electrical behavior was calculated. For this purpose, the initial resistance of the wire had to be calculated with the following equation (10):

$$R_0 = 4\rho\frac{l_0}{\pi {d_0}^2} \tag{10}$$

R_0 is the initial resistance of the sensor, ρ is the specific resistance of the wire material, l_0 is the initial length of the wire in the sensor grid and d_0 is the initial diameter. For the length calculation of the reverse loops, the formula for the circumference of the circle was applied. The following total differential was utilized to calculate the resistance change (11):

$$\Delta R = \frac{\partial R}{\partial \rho}d\rho + \frac{\partial R}{\partial l_0}dl_0 + \frac{\partial R}{\partial d_0}dd_0 \tag{11}$$

In this case, the partial derivate involving the specific resistivity ρ can be ignored, because there is no piezoresistive effect with this sensor material. The change in resistance is basically due to the change in geometry as a result of a mechanical load. The following formula for resistance change can be derived from the total differential (12):

$$\Delta R = R_0\varepsilon(1 + 2\mu) \tag{12}$$

ΔR is the resistance change of the wire, R_0 is the initial resistance of the wire from equation (10), ε is the total length change calculated from the individual ε_i from equation (9) and μ is the Poisson's ratio of the wire.

2.5 Sensor Simulation

COMSOL Multiphysics was used for the finite element method (FEM). This software enables the calculation of single physical values such as stresses and strains in structural mechanics or electric currents and fields in electrical engineering. Fully coupled simulations are possible as well. The material properties applied for the simulation are shown in **Tab. 1**.

The simulation was based on a linear elastic model using a stationary study. The calculation was performed by using isotropic properties of both materials. The computation is based on a coupled analysis between structural mechanics and electric current. The sensor was simulated in steps of 0.05 mm up to a deflection of 0.35 mm. At 0.4 mm, the yield strength of constantan would be exceeded. The mechanical stresses of the part for a deflection of 0.35 mm is shown in **Fig. 4**.

Table 1 Mechanical and electrical properties of the materials

Parameter	PETG	Constantan	Source
Yield strength	47 MPa	250 MPa	[20,21]
Young's modulus	1500 MPa	165000 MPa	[20,22]
Poisson's ratio	0.40	0.33	[23,24]
Density	1270 kg·m^{-3}	8900 kg·m^{-3}	[20,21]
Conductivity	-	4.9·10^{-7} Ω·m	[21]

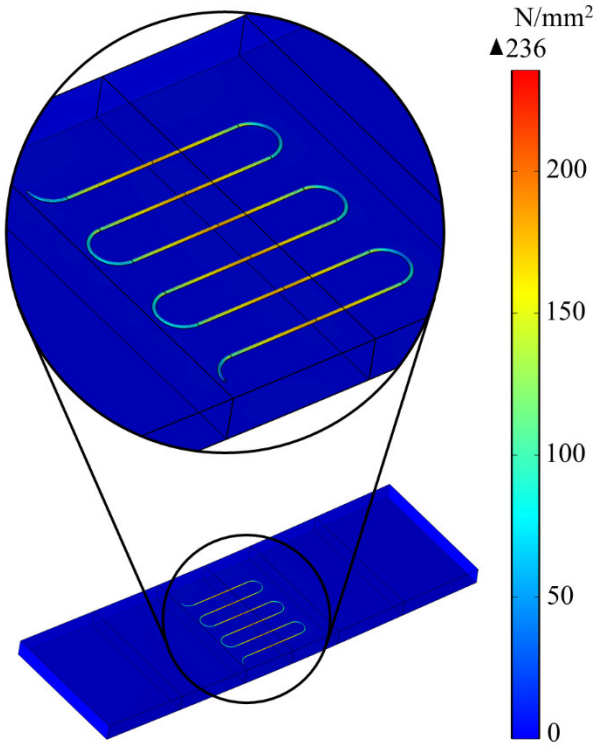

Figure 4 Simulation of the mechanical stresses of the sensor at a deflection of 0.35 mm

2.6 Sensor Fabrication

The carrier component made of PETG was fabricated with the 3D printer. During an interruption in printing, the constantan wire was embedded in the component by the robot. The setup of the system is shown in **Fig. 5**.
The layer height of the sensor is 0.2 mm at rectilinear printing pattern, 45 ° raster angle and 100 % filling density. The 3D printing was interrupted at a height of 2.6 mm for the purpose of embedding the wire. After embedding, the wire was at an average height of 2.5 mm. In a final step, two PETG top layers were applied. The printing temperature of PETG was set to 250 °C and the bed temperature to 90 °C. This corresponds to the standard settings for Prusament PETG in the PrusaSlicer. The constantan wire was heated up to 190 °C and embedded at a velocity of 2.97 mm/s. These values were determined based on preliminary tests. The industrial robot was programmed using the robotic software KeMotion from Keba.

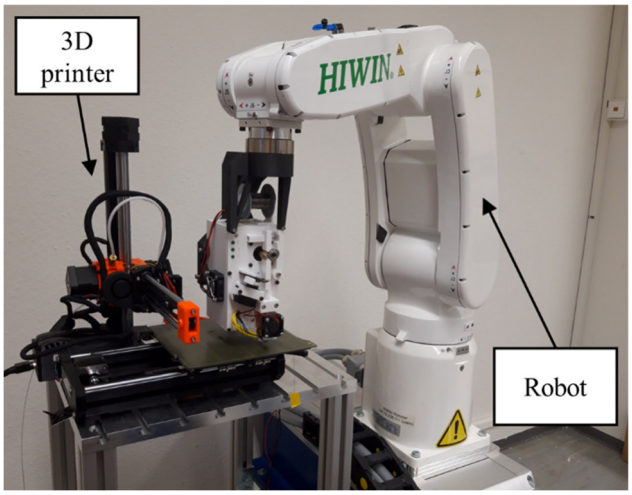

Figure 5: Setup of the system applied to fabricate the 3D printed force sensor

Fig. 6 shows the fabrication steps of the sensor after embedding the wire as well as the finished 3D printed sensor. A total of three identical sensor samples were manufactured for the experiment.

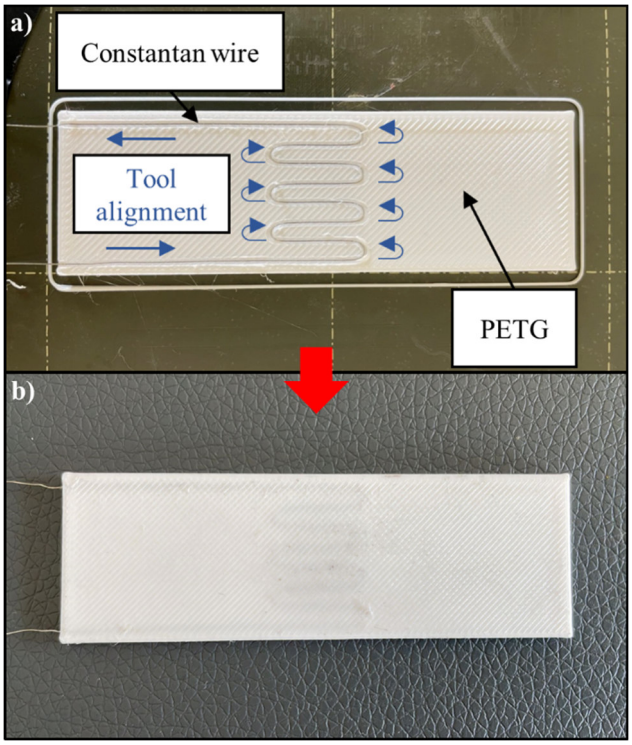

Figure 6 Fabrication of the sensor: a) Embedding the constantan wire, and b) final sensor

2.7 Experimental Setup

The Z020 universal testing machine from Zwick & Roell was used for the bending tests and force measurements. The experimental setup is shown in **Fig. 7**.

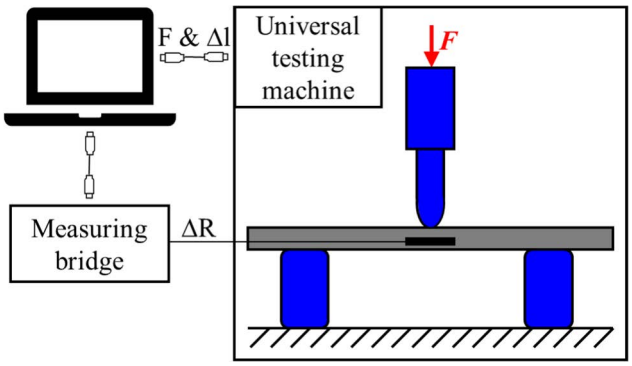

Figure 7 Experimental Setup for the three point bending test following DIN EN ISO 178

The measuring bridge ST2829C from Sourcetronic was applied for the resistance change measurement of the sensor samples. The maximum accuracy of the measurement device is achieved for slow measurement speeds of 187 ms per measurement. In order to increase the accuracy, the average value derived from 100 single measurements per cycle was calculated. The deflection was increased in single steps of 0.05 mm up to the irreversible damaging of the sensor samples. Each step was repeated three times to check the repeatability of the measurements. The resolution of the output value of the measuring device is 0.01 mΩ.

3 Results and Discussion

3.1 Verification of the measurement accuracy of the LCR-Meter

For the verification of the measurement accuracy of the ST2829C, 100 measurements were performed on an unloaded sensor sample. The measured values were found to be normally distributed, checked utilizing the Kolmogorov Smirnov Method. The null hypothesis with an error rate of 5 % served as foundation. The results are shown in **Fig. 8**. The standard deviation of the measurements is $22.6 \cdot 10^{-6}$ Ω.

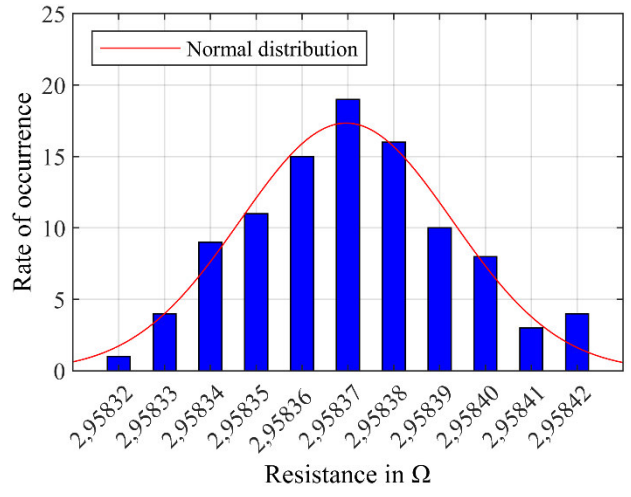

Figure 8 Measurment results and the normal distribution curve

3.2 Three-Point Bending Test

The values of the measured resistance change are shown in **Fig. 9**. The sensor was deflected in steps of 0.05 mm to 0.25 mm. The repeatability was observed up to a deflection of 0.2 mm. At a deflection of 0.2 mm or more, a deviation towards a negative resistance change occurs and the zero point is shifted. According to the simulation, a deflection of approximately 0.35 mm should be possible. This shift is probably attributable to the wire cutting into the reverse loops. In this case, the wire penetrates the material irreversibly with increasing load and destroys the sensor sample. This would also explain the shift in the negative resistance direction. In the case of plastic deformation of the sensor, the deviation should be in the positive resistance direction.

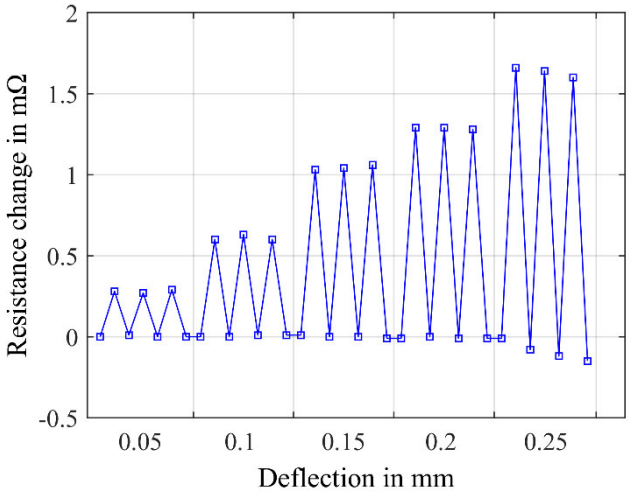

Figure 9 Resistance change for different deflections

To visualize the linear behavior of the sensor, the average values of the resistance changes were taken at the different deflections. The same was done for the applied forces resulting from the deflections. In **Fig. 10** the results of this are shown. The calculated values of the parameters from chapter 2.4 (Sensor Modeling) and chapter 2.5 (Sensor Simulation) are plotted, too.

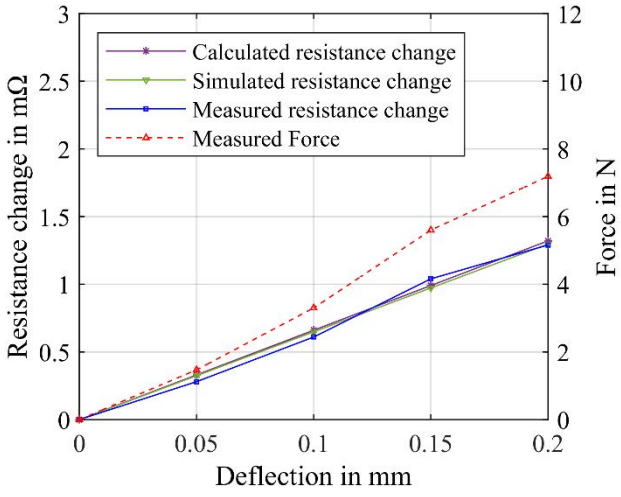

Figure 10 Behavior of the sensor with regard to linearity

The measurement results (force and resistance change) show an approximately proportional behavior to each other. Certain deviations are visible. For the comparison between the calculated and simulated values, a difference of -2.11 % can be observed. The deviation is attributed to a simplification into the mechanical calculation. For the sensor grid, the Poisson ratio of the substrate was not considered. This means that the cross contraction of the reverse loops was omitted. The difference between the simulated and measured end value is -0.21 %. The calculation and simulation based on isotropic material properties was sufficient.

3.3 Reproducibility of Different Sensor Samples

The final experiment was done in order to verify the reproducibility of additional sensor samples. For this a series of three samples were prepared and tested. The results are shown in **Fig. 11**.
Sensor sample 2 showed an average peak of 0.18 mΩ at 0.05 mm, which is 34.64 % lower than sensor sample 1. Sensor sample 3 showed an average peak of 0.87 mΩ at 0.15 mm, which is 16.35 % lower than sensor sample 1. The deviations of the resistance changes of sensor sample 3 compared to sensor sample 1 increased further beyond a deflection of 0,15 mm. Except for the discrepancies mentioned above, the reproducibility is well. The values of the sensor samples are almost identical with each other. The differences in resistance changes are related to the manufacturing tolerance of the individual sensor samples. The low value of sensor sample 2 at 0.05 mm may indicative of a warped component and wire. The failure of sensor sample 3 at an early stage could be related to an early wire cutting into the reverse loops. Alternatively, the wire may also have slipped.

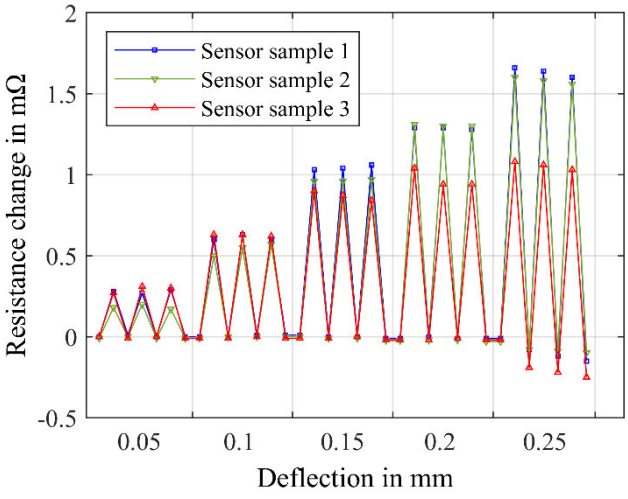

Figure 11 Resistance change for different deflections of various sensor samples

4 Conclusion and Outlook

A force sensor with an integrated constantan wire as the sensing element was modeled, simulated, fabricated and verified. The results of the measurements confirmed the results of the previously performed calculation and simulation. The small differences between the calculated and simulated values are attributed to a simplification into the mechanical calculation.
The sensor fabricated in this work serves as the basis for an integration into a robotic gripping system. In addition to the integration of the sensor in gripper jaws, further properties are to be investigated. The creep behavior and durability of the sensor type should be analyzed to determine the improved suitability of these sensors compared to sensors consisting of conductive plastic or silver inks. For better expected reproducibility of the sensor samples, the tool for embedding the wire is to be integrated into the Neotech AMT 15X SA.

5 Acknowledgement

Funded by the Federal Ministry for Economic Affairs and Energy in the Central Innovation Program for small and medium-sized enterprises (SMEs).

6 Literature

[1] T. Aaklint, E. Carlstroem, P. Johander, and J. Stiernstedt, “LAYERED MANUFACTURING OF FREE-FORM MULTI-MATERIAL MICRO-COMPONENTS,” WO2013030064 (A1), WO WO2012EP66339 20120822, Mar 7, 2013.

[2] J. Qu, Q. Wu, T. Clancy, and X. Liu, “Design and calibration of 3D-printed micro force sensors,” in 2016 International Conference on Manipulation, Automation and Robotics at Small Scales (MARSS), Paris, France, 72016, pp. 1–4.

[3] J. A. Lewis, M. A. Bell, T. A. Busbee, J. E. Minardi, and J. E. Minardi, II, “PRINTED THREE-DIMENSIONAL (3D) FUNCTIONAL PART AND METHOD OF MAKING,” US2016198576 (A1), US US201414900860 20140624, Jul 7, 2016.

[4] K.-Y. Joung, S.-Y. Kim, I. Kang, and S.-H. Cho, “3D-Printed Load Cell Using Nanocarbon Composite Strain Sensor,” Sensors (Basel, Switzerland), vol. 21, no. 11, 2021, doi: 10.3390/s21113675.

[5] Y. Song, R. A. Boekraad, L. Roussos, A. Kooijman, C. C. L. Wang, and J. M. P. Geraedts, “3D Printed Electronics: Opportunities and Challenges From Case Studies,” in Volume 1: 37th Computers and Information in Engineering Conference, Cleveland, Ohio, USA, 2017.

[6] N. Hangst, S. Junk, and T. Wendt, “Verfahren zur Herstellung eines Roboterelements, insbesondere eines Greifers, mittels 3D-Druck,” US2020247044 (A1), US US202016776973 20200130, Aug 6, 2020.

[7] S. Junk and N. Hangst, “Einsatz von 3D-Multimaterialdruck zur schnellen Herstellung von multifunktionalen Mensch-Roboter-Kollaborations-Greifsystemen,” in Fachtagung Werkstoffe und Additive Fertigung: 25.-26.04.2018, Potsdam : Tagungsband, P. Hoyer, C. Leyens, T. Niendorf, V. Ploshikhin, V. Schulze, and G. Wtt, Eds., 2018, pp. 115–120.

[8] T. Wendt, N. Hangst, P. Gawron, and S. Junk, “3D-Druck von leitfähigen Materialien bei gedruckter Sensorik in intelligenten und multifunktional aufgebauten Mensch-Roboter-Kollaborations-Greifsystemen,” in Sensoren und Messsysteme: Beiträge der 19. ITG/GMA-Fachtagung, 26-27 Juni 2018 in Nürnberg, Frankfurt am Main: VDE, 2018, pp. 135–138.

[9] M. N. Saadatzi, S. K. Das, I. B. Wijayasinghe, D. O. Popa, and J. R. Baptist, “Precision Grasp Control with a Pneumatic Gripper and a Novel Fingertip Force Sensor,” in 2018 IEEE 14th International Conference on Automation Science and Engineering (CASE), Munich, Germany, 82018, pp. 1454–1459.

[10] N. Hangst, S. Junk, and T. Wendt, “Design of an Additively Manufactured Customized Gripper System for Human Robot Collaboration,” in Industrializing additive manufacturing: Proceedings of AMPA2020, M. Meboldt and C. Klahn, Eds., Cham, Switzerland: Springer, 2021, pp. 415–425.

[11] L. Kaiser, A. Schlotzhauer, and M. Brandstötter, “Safety-Related Risks and Opportunities of Key Design-Aspects for Industrial Human-Robot Collaboration,” in Lecture Notes in Computer Science, Interactive Collaborative Robotics, A. Ronzhin, G. Rigoll, and R. Meshcheryakov, Eds., Cham: Springer International Publishing, 2018, pp. 95–104.

[12] R. Becker and A. Grzesiak, “Robot grip for manipulating articles has at least fixing flange, frame and actuator element made in one piece,” DE102005046160 (B3), DE DE20051046160 20050927, Mar 22, 2007.

[13] R. R. Dehoff, R. F. Lind, L. L. Love, W. H. Peter, and B. S. Richardson, “FREEFORM FLUIDICS,” US2013331949 (A1), US US201213493683 20120611, Dec 12, 2013.

[14] D. Rau, M. R. Burhop, R. Williams, E. Arvanitis, and L. Dalloro, “CUSTOMIZED ROBOTIC GRIPPERS WITH FEEDBACK SENSORS,” WO2020041221 (A1), WO WO2019US47124 20190820, Feb 27, 2020.

[15] A. Georgopoulou, B. Vanderborght, and F. Clemens, “Multi-material 3D Printing of Thermoplastic Elastomers for Development of Soft Robotic Structures with Integrated Sensor Elements,” in Industrializing additive manufacturing: Proceedings of AMPA2020, M. Meboldt and C. Klahn, Eds., Cham, Switzerland: Springer, 2021, pp. 67–81.

[16] A. N. Dickson, J. N. Barry, K. A. McDonnell, and D. P. Dowling, “Fabrication of continuous carbon, glass and Kevlar fibre reinforced polymer composites using additive manufacturing,” Additive Manufacturing, vol. 16, pp. 146–152, 2017, doi: 10.1016/j.addma.2017.06.004.

[17] T. Kies, 10 Grundregeln zur Konstruktion von Kunststoffprodukten, 2nd ed. München: Carl Hanser Verlag, 2018.

[18] A. Al Rashid and M. Koç, “Creep and Recovery Behavior of Continuous Fiber-Reinforced 3DP Composites,” Polymers, vol. 13, no. 10, 2021, doi: 10.3390/polym13101644.

[19] J. L. Faust, P. G. Kelly, B. D. Jones, and J. D. Roy-Mayhew, “Effects of Coefficient of Thermal Expansion and Moisture Absorption on the Dimensional Accuracy of Carbon-Reinforced 3D Printed Parts,” Polymers, vol. 13, no. 21, 2021, doi: 10.3390/polym13213637.

[20] Prusa Research s.r.o.,” Technical Data Sheet Prusament PETG,” 2020. Accessed: Apr. 1 2021. [Online]. Available: https://prusament.com/media/2020/01/PETG_TechSheet_ENG.pdf.

[21] Ualloy Material Co., Ltd.,” Technical Data Sheet CuNi44”. Accessed: Apr. 1 2021. [Online]. Available: http://de.alloystrip.com/copper-based-alloy/copper-nickel-alloy/copper-nickel-alloy-cuni44.html.

[22] Schlenk GmbH & Co. KG,” Technical Data Sheet CuNi44”. Accessed: Apr. 1 2021. [Online]. Available: https://de.schlenk.com/fileadmin/editorsCMS/uploads/PDF/Metallfolien_Datenbl%C3%A4tter_Kataloge/Deutsch/CuNi44.pdf.

[23] S. Guessasma, S. Belhabib, and H. Nouri, “Printability and Tensile Performance of 3D Printed Polyethylene Terephthalate Glycol Using Fused Deposition Modelling,” Polymers, vol. 11, no. 7, 2019, doi: 10.3390/polym11071220.

[24] MakeltFrom,” Technical Data Sheet CuNi44”. Accessed: Apr. 1 2021. [Online]. Available: https://www.makeitfrom.com/material-properties/UNS-C72150-CuNi44-Copper-Nickel.